


Dynamics of elliptical vortices with continuous profiles

Ling Xu ^{*}*Department of Mathematics and Statistics, North Carolina Agricultural and Technical State University,
Greensboro, North Carolina 27411, USA*Robert Krasny [†]*Department of Mathematics, University of Michigan, Ann Arbor 48109, Michigan, USA*

(Received 7 July 2022; accepted 2 February 2023; published 21 February 2023)

This work examines the dynamics of elliptical vortices in two-dimensional ideal fluid using an adaptively refined and remeshed vortex method. Four examples are considered comprising two compact vortices denoted by MMZ (smooth) and POLY (nonsmooth), and two noncompact vortices denoted by Gaussian and smooth Kirchhoff. The vortices all have the same maximum vorticity and 2:1 initial aspect ratio, but unlike the top-hat Kirchhoff vortex, they have continuous profiles with different degrees of regularity. In each case the phase portrait of the vortex in a corotating frame has two hyperbolic points, and the separatrix divides space into four regions, a center containing the vortex core, two crescent-shaped lobes next to the core, and the exterior. As the vortices start to rotate, two spiral filaments emerge and form a halo of low-amplitude vorticity around the core; this is attributed to vorticity advection along the unstable manifolds of the hyperbolic points. In the case of the Gaussian vortex the core rapidly axisymmetrizes, but later it starts to oscillate and two small lobes enclosing weak vortical fluid form within the halo; this is attributed to a resonance stemming from the core oscillation. In the case of the MMZ, POLY, and smooth Kirchhoff vortices, the core remains elliptical for longer time, and the filaments entrain weak vortical fluid into two large lobes which together with the core form a nonaxisymmetric tripole; afterwards, however, the lobes repeatedly detrains some of their fluid into the halo; the repeated detrainment is attributed to a heteroclinic tangle near the hyperbolic points. While prior work suggested that elliptical vortices could evolve to become either an axisymmetric monopole or a nonaxisymmetric tripole, the current results suggest they may oscillate between these states.

DOI: [10.1103/PhysRevFluids.8.024702](https://doi.org/10.1103/PhysRevFluids.8.024702)

I. INTRODUCTION

The dynamics of elliptical vortices is a topic of longstanding interest in fluid and plasma dynamics. The simplest example is the Kirchhoff vortex with a discontinuous top-hat profile having uniform vorticity inside an ellipse and zero vorticity outside and which rotates with constant angular velocity in two-dimensional (2D) ideal fluid [1,2]. Love [3] showed that the Kirchhoff vortex is linearly stable for aspect ratio less than three. The nonlinear stability of the Kirchhoff vortex can be studied through contour dynamics simulations [4,5], and in this way Mitchell and Rossi [6] computed cases with high aspect ratio where the perturbed vortex splits into compact regions connected by thin filaments.

*lxu@ncat.edu

†krasny@umich.edu

In contrast to the Kirchhoff vortex, the present work is concerned with elliptical vortices having continuous vorticity profiles. While several studies considered such vortices in an external strain field [7–11], or having nonmonotone profiles with opposite-sign vorticity [12], we focus on freely evolving vortices with monotone single-sign profiles. For context, the following subsections briefly review some of the many previous studies of elliptical vortices.

A. Experimental studies

Elliptical vortices have been studied experimentally in rotating fluids and magnetically confined electron plasmas, where the electron density is analogous to the fluid vorticity. In a rotating fluid experiment initialized with a compact axisymmetric vortex, van Heijst *et al.* [13] observed the formation of a tripole structure with an elliptical core surrounded by two crescent-shaped lobes having opposite-sign vorticity to the core. In the case of plasma experiments, Briggs *et al.* [14] found that neutrally stable normal modes exist for top-hat electron density profiles, but these modes disappear when the profile is smoothed. Driscoll and Fine [15] showed that a large-amplitude elliptical perturbation of the Kirchhoff vortex evolves into a tripole structure in which the lobes have low-amplitude electron density. Schecter *et al.* [16] considered elliptically perturbed top-hat and Gaussian electron density profiles; their experimental and theoretical study showed that the ellipticity of the vortex decays exponentially at early times due to inviscid damping, but while the theory predicts a transition to algebraic decay at later times, the experiments instead displayed saturated oscillations.

B. Analytical studies

Elliptical vortices have been studied extensively by linear stability theory and weakly nonlinear asymptotics. Bernoff and Lingeitch [17] found that an elliptically perturbed Gaussian vortex in high Reynolds number flow rapidly relaxes to an axisymmetric state due to differential rotation and viscous diffusion. Bassom and Gilbert [18] studied the spiral wind-up of vorticity filaments around an azimuthally perturbed smooth inviscid vortex and found that the vorticity tends to axisymmetry in the sense of weak convergence at a rate that depends on the perturbation wave number. Le Dizès [19] studied elliptical perturbations of axisymmetric viscous vortices with a flat plateau and Gaussian decay and showed there is a threshold amplitude depending on the Reynolds number below which the vortex returns to an axisymmetric state and above which a critical layer forms leading to a nonaxisymmetric tripole. Balmforth *et al.* [20] considered a family of compact vortices approximating a Gaussian profile and showed that for elliptical perturbations of sufficient amplitude, nonlinearity prevents the perturbation from decaying and the vortex tends to a nonaxisymmetric tripole. Hall *et al.* [21] studied inviscid vortices with a sharp edge and showed that as the edge vorticity profile becomes steeper, a decaying quasimode emerges and vorticity winds up in a critical layer; moreover when additional fine structure is present in the critical layer, the quasimode may be destabilized and exhibit oscillatory behavior. Turner and Gilbert [22] applied the asymptotic theory of Balmforth *et al.* [20] to determine a threshold amplitude for the persistence of satellite vortices around a compact vortex perturbed by an elliptical skirt of weak vorticity.

In addition to linear stability theory and weakly nonlinear asymptotics, several other analytical methods have been applied to study elliptical vortices. For example, Whitaker and Turkington [23] applied statistical equilibrium theory to elliptical vortices evolving in a circular disk and showed that in the case of large disks, the maximum entropy state is axisymmetric, while Bedrossian *et al.* [24] rigorously proved that axisymmetrization occurs by inviscid damping in the linearized 2D Euler equations for vortices having smooth monotone profiles.

C. Computational studies

The nonlinear dynamics of elliptical vortices has been studied in several direct numerical simulations using various computational techniques. Melander *et al.* [25] simulated a smooth compact elliptical vortex (denoted MMZ) in weakly dissipative fluid using a pseudospectral method; as the

vortex starts to rotate, two filaments emerge from the tips and wrap around the core; a nonaxisymmetric tripole develops with an elliptical core surrounded by two crescent-shaped lobes enclosing irrotational fluid, but over time the structure tends to axisymmetrize. Dritschel [26] considered a compact parabolic vorticity profile represented by nested elliptical contours and used contour dynamics with surgery to track the evolution, obtaining qualitatively similar results to those of Melander *et al.* [25]; however, calculations with a steeper fourth degree polynomial profile showed more persistent nonaxisymmetrization [27]. Polvani *et al.* [28] studied a perturbed Kirchhoff vortex using contour dynamics; they noted that the phase portrait in the corotating frame has two hyperbolic points; in the unperturbed case where the ellipse rotates without change in shape, the hyperbolic points lie outside the vortex, but during the evolution of the perturbed ellipse, one of the hyperbolic points enters the vortex and this results in filamentation of the vortex boundary. Koumoutsakos [29] studied inviscid elliptical vortices using a remeshed vortex method; two examples were considered, the MMZ profile and a compact fourth degree polynomial profile [27] (denoted POLY); as seen previously, the MMZ vortex tends to axisymmetrize [25], but the POLY vortex evolves into a nonaxisymmetric tripole similar to that in the plasma experiment of Driscoll and Fine [15]. Rossi *et al.* [30] computed the viscous evolution of elliptically perturbed Gaussian vortices using the corrected core-spreading vortex method; they found there is a threshold perturbation amplitude below which the vortex tends to an axisymmetric state and above which it tends to a quasisteady rotating tripole. Dritschel [31] studied inviscid elliptical vortices having a parabolic profile with a discontinuity at the edge using the contour-advective semi-Lagrangian method and found that vortices with sufficiently steep edges can remain nonaxisymmetric indefinitely. Velasco Fuentes [32] performed inviscid vortex-in-cell calculations of a perturbed Kirchhoff vortex and several compact polynomial profiles; the results show that filamentation can start even when the hyperbolic point is outside the vortex, and subsequently the filament is advected along the unstable manifold of the hyperbolic point. Barba and Leonard [33] considered initial vorticity consisting of a Gaussian monopole with an elliptical perturbation; they studied the viscous evolution using a core-spreading vortex method with spatial adaption by radial basis function interpolation; the results show there is a threshold perturbation amplitude depending on the Reynolds number below which the vortex tends to an axisymmetric state and above which it tends to a tripole state. Pakter and Levin [34] and Farias *et al.* [35] did point vortex and vortex-in-cell simulations of a perturbed Kirchhoff vortex and observed the formation of a nonaxisymmetric tripole with an elliptical core surrounded by a halo of weak vorticity in a thin layer around the unperturbed separatrix.

To summarize, the previous computational studies have investigated several different elliptical vorticity profiles using spectral methods, contour dynamics, and vortex methods. Depending on the initial profile characteristics and perturbation amplitude, in some cases the vortex tends to axisymmetrize, whereas in other cases it evolves to a long-lived tripole state which could in principle eventually tend to axisymmetrize on a longer timescale. The present work therefore seeks to further study this issue.

D. Present work

The present work reexamines the dynamics of elliptical vortices using an adaptively refined and remeshed vortex method [36,37]. Chorin [38] introduced the vortex method for incompressible fluid simulations, and several reviews describe later developments [39–41]. In this method the vorticity is carried by Lagrangian particles and the velocity is obtained by evaluating a smoothed form of the Biot-Savart integral. The accuracy and stability of the method depend on the relation between the smoothing parameter and the particle spacing [42,43]. Perlman [44] showed that the accuracy of these calculations can deteriorate when the particles become disordered, and remeshing methods were developed to overcome this problem [29,40,45].

Four vorticity profiles are considered here, the compact Melander-McWilliams-Zabusky (MMZ) [25] and polynomial (POLY) [29] profiles, and noncompact Gaussian (G) and smoothed Kirchhoff (SK) profiles. The profiles are continuous, although with different regularity, and they are elliptically

stretched so that the initial vorticity distribution has 2:1 aspect ratio as in prior work [25,29]. In addition to vorticity snapshots at various times, movies are presented to show what happens between the snapshots.

In all four cases as the vortices start to rotate, two filaments emerge and form a halo of low-amplitude vorticity outside the core, but the subsequent evolution depends on the profile. In the case of the Gaussian vortex, the core rapidly axisymmetrizes and the filaments form nearly circular spirals, but later on two small lobes enclosing weak vortical fluid form within the halo. In the case of the MMZ, POLY, and SK vortices, the core remains elliptical for longer time and the filaments entrain fluid into two large lobes which together with the core form a nonaxisymmetric tripole; afterwards the lobes repeatedly detrain some of their fluid into the halo. Throughout this work we seek to understand these computational observations by reference to dynamical systems theory.

The paper is organized as follows. Section II presents the governing equations, Sec. III recalls the phase portrait of the Kirchhoff vortex, Sec. IV presents the four continuous vorticity profiles, Sec. V describes the version of the vortex method used here, Sec. VI presents the numerical results, and Sec. IX provides a summary.

II. GOVERNING EQUATIONS

The Eulerian formulation of vortex dynamics in 2D ideal fluid relates the vorticity $\omega(\mathbf{x}, t)$, velocity $\mathbf{u}(\mathbf{x}, t)$, and stream function $\psi(\mathbf{x}, t)$,

$$\frac{\partial \omega}{\partial t} + \mathbf{u} \cdot \nabla \omega = 0, \quad \mathbf{u} = \nabla^\perp \psi, \quad \nabla^2 \psi = -\omega, \quad \mathbf{x} = (x, y) \in \mathbb{R}^2. \quad (1)$$

The Lagrangian formulation specifies the evolution of the flow map $\mathbf{x}(\mathbf{a}, t)$, which gives the location at time t of the fluid particle initially located at $\mathbf{x}(\mathbf{a}, 0) = \mathbf{a}$ [46]. The velocity of a fluid particle following the flow is given by the Biot-Savart integral,

$$\frac{\partial \mathbf{x}(\mathbf{a}, t)}{\partial t} = \int_{\mathbb{R}^2} \mathbf{K}(\mathbf{x}(\mathbf{a}, t), \mathbf{x}(\mathbf{b}, t)) \omega_0(\mathbf{b}) d\mathbf{b}, \quad (2)$$

where the kernel is

$$\mathbf{K}(\mathbf{x}, \mathbf{y}) = \nabla_{\mathbf{x}}^\perp G(\mathbf{x}, \mathbf{y}), \quad (3)$$

and the 2D Laplace Green's function is

$$G(\mathbf{x}, \mathbf{y}) = -\frac{1}{2\pi} \ln |\mathbf{x} - \mathbf{y}|. \quad (4)$$

This formulation utilizes the fact that the vorticity is conserved on particle trajectories, $\omega(\mathbf{x}(\mathbf{a}, t), t) = \omega_0(\mathbf{a})$.

III. KIRCHHOFF VORTEX

The Kirchhoff vortex is recalled here for reference; it has uniform vorticity inside an ellipse and zero vorticity outside [1,2],

$$\omega_K(x, y) = \begin{cases} \omega_{\max}, & r \leq 1, \\ 0, & r > 1, \end{cases} \quad r = \left(\frac{x^2}{a^2} + \frac{y^2}{b^2} \right)^{1/2}, \quad (5)$$

where we take $\omega_{\max} > 0$, r is the stretched radius, and a, b are the ellipse semiminor and semimajor axes with $0 < a < b$. The Kirchhoff vortex rotates with constant angular velocity,

$$\Omega = \omega_{\max} \frac{ab}{(a+b)^2}, \quad (6)$$

and retains its elliptical shape.

Figure 1(a) shows the phase portrait of the Kirchhoff vortex in the corotating frame with $a = 0.8$, $b = 1.6$ yielding 2:1 aspect ratio, comprising the separatrix (red), streamlines (green), vortex

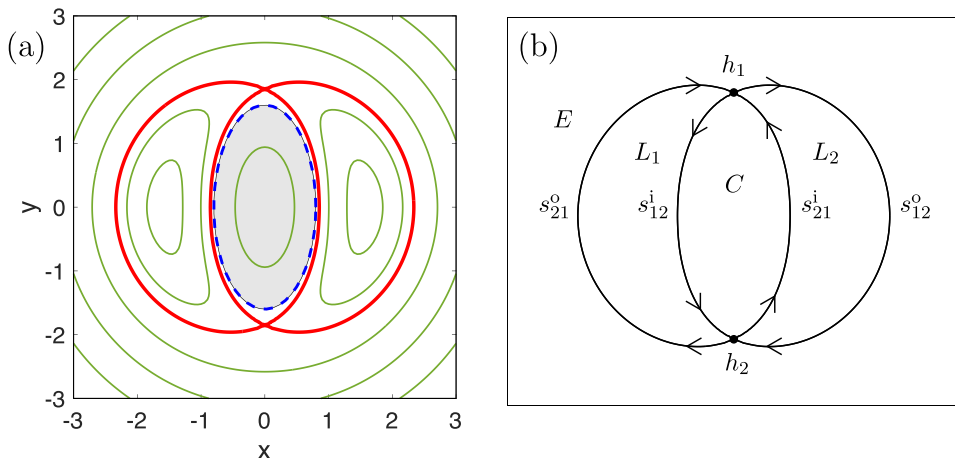


FIG. 1. Phase portrait of Kirchhoff vortex in corotating frame, 2:1 aspect ratio. (a) Separatrix (red), streamlines (green), vortex (shaded gray), and vortex boundary (dashed blue); (b) two hyperbolic points h_1, h_2 , four heteroclinic orbits, inner and outer orbits s_{12}^i, s_{12}^o from h_1 to h_2 , inner and outer orbits s_{21}^i, s_{21}^o from h_2 to h_1 , four invariant regions, center C , lobes L_1, L_2 , and exterior E .

(shaded gray), and vortex boundary (dashed blue). Figure 1(b) defines features of the phase portrait, two hyperbolic points h_1, h_2 on the ellipse major axis outside the vortex, and four heteroclinic orbits comprising inner and outer orbits s_{12}^i, s_{12}^o from h_1 to h_2 , and inner and outer orbits s_{21}^i, s_{21}^o from h_2 to h_1 . The heteroclinic orbits define the stable and unstable manifolds of the hyperbolic points.

The separatrix divides space into four invariant regions, the center C , two crescent-shaped lobes L_1, L_2 , and exterior E . The boundary of the vortex comes close to the separatrix, but it is contained entirely within the center region. The lobes and exterior contain irrotational fluid. In the corotating frame, the fluid rotates counterclockwise in the center, and clockwise in the lobes and exterior, and the hence phase portrait may be considered as having a tripole structure. The Kirchhoff vortex is steady in the corotating frame and there is no exchange of fluid among the four regions. However, in the case of unsteady elliptical vortices, while the instantaneous phase portrait has the same topology as Fig. 1, the dynamics can be more complex; the stable and unstable manifolds of the hyperbolic points can intersect, resulting in a heteroclinic tangle that permits an exchange of fluid among the regions, and resonances can occur in the regions with closed streamlines [47–50]. We shall see some evidence of this in the simulations below.

IV. CONTINUOUS VORTICITY PROFILES

This work examines the dynamics of four elliptical vortices with continuous profiles: Gaussian (G), MMZ [25], POLY [29], and SK. The initial vorticity distributions are

$$\omega_G(\mathbf{x}) = \omega_{\max} \exp(-12r^2), \quad r \geq 0, \quad (7a)$$

$$\omega_{\text{MMZ}}(\mathbf{x}) = \begin{cases} \omega_{\max} \left\{ 1 - \exp\left[-\frac{q}{r} \exp\left(\frac{1}{r-1}\right)\right] \right\}, & r \leq 1, \\ 0, & r > 1, \end{cases} \quad (7b)$$

$$\omega_{\text{POLY}}(\mathbf{x}) = \begin{cases} \omega_{\max}(1 - r^4), & r \leq 1, \\ 0, & r > 1, \end{cases} \quad (7c)$$

$$\omega_{\text{SK}}(\mathbf{x}) = \int_{\mathbb{R}^2} -\nabla_{\mathbf{x}}^2 G_{\delta}(\mathbf{x}, \mathbf{y}) \omega_K(\mathbf{y}) d\mathbf{y}, \quad (7d)$$

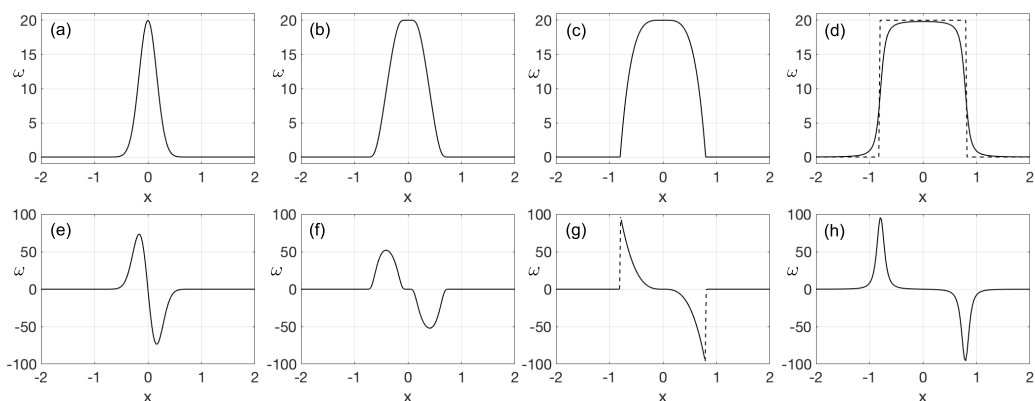


FIG. 2. Vorticity profiles (top) and derivatives (bottom) of elliptical vortices from Eq. (7) along the x axis, [(a) and (e)] Gaussian, [(b) and (f)] MMZ, [(c) and (g)] POLY, and [(d) and (h)] smooth Kirchhoff with smoothing parameter $\delta = 0.1$, dashed lines in (g) indicate discontinuity, Kirchhoff vortex shown as dashed lines in (d).

where r is the stretched radius defined in Eq. (5). Note that $\omega_{\text{MMZ}}(\mathbf{x})$ is computed with constant $q = 0.5e^2 \ln 2 \approx 2.57$ [25], and $\omega_{\text{SK}}(\mathbf{x})$ is obtained by convolving the top-hat Kirchhoff vortex $\omega_K(\mathbf{x})$ from Eq. (5) with an approximate delta function $-\nabla_y^2 G_\delta(\mathbf{x}, \mathbf{y})$, where

$$G_\delta(\mathbf{x}, \mathbf{y}) = -\frac{1}{4\pi} \ln(|\mathbf{x} - \mathbf{y}|^2 + \delta^2) \quad (8)$$

is a regularized form of the Green's function in Eq. (4) and the convolution is computed numerically with smoothing parameter $\delta = 0.1$. The maximum vorticity is $\omega_{\text{max}} = 20$, and the semiminor and semimajor axes are $a = 0.8$, $b = 1.6$, so the vortices have 2:1 initial aspect ratio [25,29]. Note that this form of elliptical perturbation using a stretched radius ensures that the vorticity remains positive, in contrast to additive perturbations that introduce satellites having opposite-sign vorticity to that in the core [22,30,33].

Figure 2 plots the vorticity profiles (top) along the x axis and their derivatives (bottom). The MMZ and POLY vortices have compact support, while the Gaussian and SK vortices have non-compact support and are nonzero on the entire plane. The Gaussian vortex decays rapidly and the SK vortex decays slowly as $|\mathbf{x}| \rightarrow \infty$. The vorticity profiles are continuous, but they have different regularity; the Gaussian and SK vortices are analytic everywhere, the MMZ vortex is infinitely differentiable but nonanalytic at the boundary, and the POLY vortex has a discontinuous derivative at the boundary. The Gaussian vortex essentially has no plateau, while the MMZ, POLY, and SK vortices have progressively wider plateaus. Using the maximum derivative as a measure of steepness, the POLY and SK vortices have the steepest profiles, followed by the Gaussian vortex, and then the MMZ vortex. While the vortices have the same maximum vorticity, they have different total circulation, $\Gamma_G = 6.70$, $\Gamma_{\text{MMZ}} = 22.12$, $\Gamma_{\text{POLY}} = 53.62$, $\Gamma_{\text{SK}} = 80.14$; for reference the Kirchhoff vortex has total circulation $\Gamma_K = \omega_{\text{max}}\pi ab = 80.42$.

Figure 3 shows the phase portraits of the elliptical vortices in a corotating frame with the separatrix (red), streamlines (green), vorticity (shaded gray), vorticity contours (blue), and the boundary of the compact MMZ and POLY vortices (dashed blue). The caption gives the rotation rate Ω used for each vortex which was determined empirically by trial and error. In all cases the phase portrait has the same topology as the Kirchhoff vortex in Fig. 1, with a center region, two lobes, and the exterior. The separatrix is smallest for the Gaussian vortex and increases in size for the MMZ, POLY, and SK vortices. Outside the separatrix the streamlines are almost circular in all cases. Unlike the Kirchhoff vortex where the hyperbolic points lie outside the vortex, they lie inside

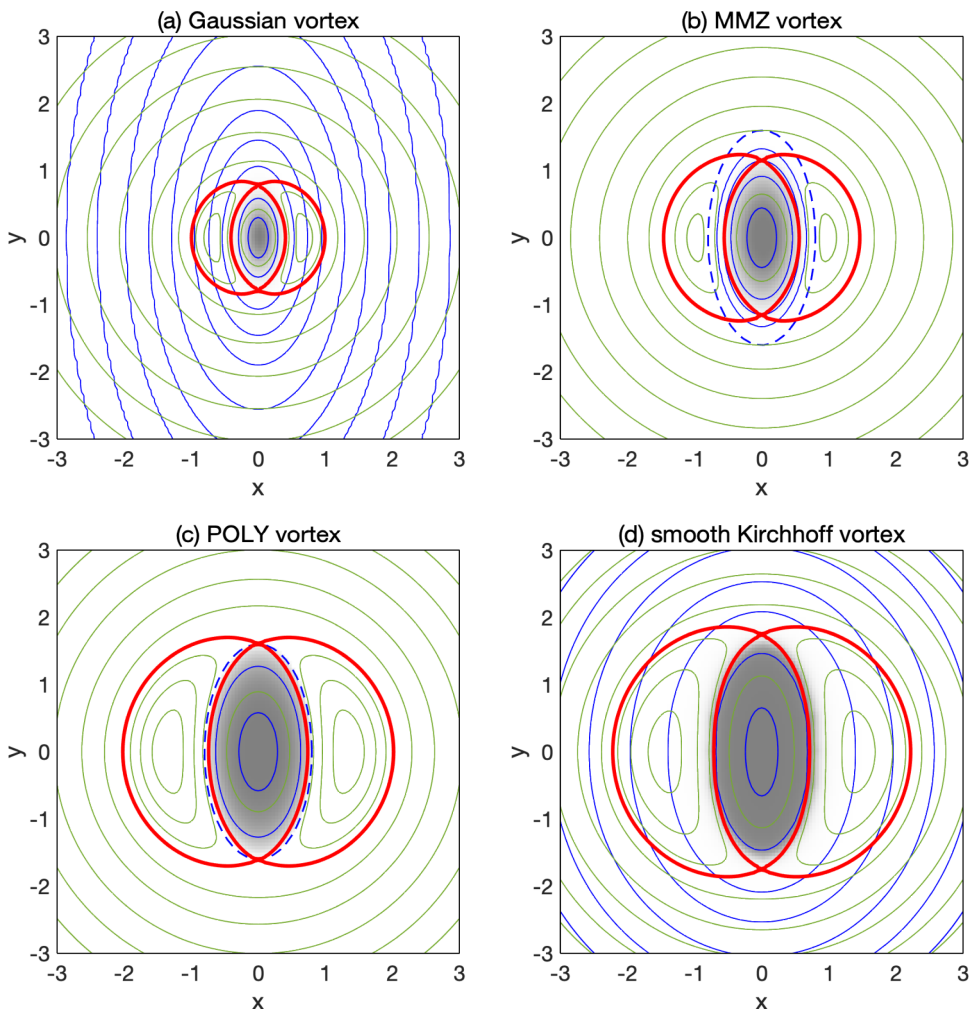


FIG. 3. Phase portraits of elliptical vortices from Eq. (7) in corotating frame, angular velocity Ω , separatrix (red), streamlines (green), vorticity (shaded gray), vorticity contours (blue), boundary of compact MMZ and POLY vortices (dashed blue), (a) Gaussian, $\Omega = 2$, (b) MMZ, $\Omega = 3.14$, (c) POLY, $\Omega = 3.9$, and (d) smooth Kirchhoff, $\Omega = \omega_{\max}ab/(a+b)^2 = 4.4$.

the MMZ vortex, on the edge of the POLY vortex, and inside the Gaussian and SK vortices (by default); this is important because filamentation occurs when the hyperbolic points lie inside the vortex [25,28] or even outside but close to the vortex in unsteady cases [32]. Note also the location of the heteroclinic orbits; the outer orbits (s_{12}^o, s_{21}^o) cut through the support of the Gaussian, MMZ, and SK vortices but not the POLY vortex, while the inner orbits (s_{12}^i, s_{21}^i) lie entirely inside the vortex support in all four cases, although for the POLY vortex they are very close to the edge.

V. VORTEX METHOD

The vortex method is based on the Lagrangian formulation of vortex dynamics given in Eq. (2) [40,46]. There are several versions of the vortex method; one version, called the vortex-in-cell (VIC) method, is essentially the same as the particle-in-cell (PIC) method popular in plasma physics [51–53], where particles are tracked in physical space (VIC) or phase space (PIC) and the fields are

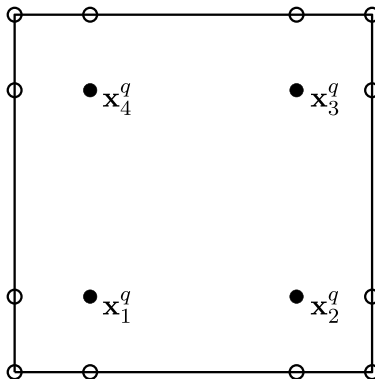


FIG. 4. Panel with 4×4 tensor product particle grid, 12 boundary particles (\circ), 4 interior particles (\bullet) denoted \mathbf{x}_j^q , $j = 1:4$, nonvertex particles have one or two coordinates at two-point Gaussian quadrature nodes.

computed using grid-based solvers. The present version of the vortex method also tracks particles, but it uses a Biot-Savart-treecode field solver on adaptively refined panels. The sections below describe the present vortex method comprising the particle and panel representation of the flow map, the remeshing scheme, a convergence study for circular vortices, the domain focusing and adaptive refinement schemes, and, finally, the treecode.

A. Particle and panel representation

The flow map is represented by Lagrangian particles, $\mathbf{x}_i(t) \approx \mathbf{x}(\mathbf{a}_i, t)$, for $i = 1 : N$, where \mathbf{a}_i is the initial particle position, $\mathbf{x}_i(0) = \mathbf{a}_i$, and each particle carries its initial vorticity, $\omega_i = \omega_0(\mathbf{a}_i)$. The computational domain $[-L, L]^2$ is discretized into square panels with mesh size h , and the panels are indexed by $k = 1 : N_{\text{panel}}$. As shown in Fig. 4, each panel has a 4×4 tensor product particle grid, where there are four vertex particles and the remaining particles have one or two coordinates given by the two-point Gaussian quadrature nodes. The four interior particles, denoted \mathbf{x}_j^q , $j = 1 : 4$, are the quadrature points used in computing the Biot-Savart integral, and the entire 4×4 particle grid is used in the remeshing and adaptive refinement schemes described below.

The flow map Eq. (2) then takes the discrete form,

$$\frac{d\mathbf{x}_i}{dt} = \sum_{k=1}^{N_{\text{panel}}} \sum_{j=1}^4 \mathbf{K}_\delta(\mathbf{x}_i, \mathbf{x}_j^q) \omega_j^q A_k, \quad i = 1 : N, \quad (9a)$$

$$\mathbf{K}_\delta(\mathbf{x}, \mathbf{y}) = \nabla_{\mathbf{x}}^\perp G_\delta(\mathbf{x}, \mathbf{y}), \quad (9b)$$

where the singular Biot-Savart kernel is replaced by a regularized version utilizing Eq. (8), the Biot-Savart integral is written as a sum over panels, the integral over each panel is computed by tensor product two-point Gaussian quadrature, ω_j^q is the vorticity carried by particle \mathbf{x}_j^q , and A_k accounts for the panel area and Gaussian quadrature weights. Equation (9) is a system of ordinary differential equations for the motion of the particles which is solved by the fourth-order Runge-Kutta method with time step given below in Table I.

B. Remeshing

In the vortex method described above the panels initially form a regular mesh to ensure the accuracy of the quadrature scheme, but as the particles evolve, they typically become disordered and the calculation loses accuracy [44]. To overcome this problem, remeshing schemes were developed [29,40,54]; before the particles become too disordered they are replaced by new particles on a

TABLE I. Numerical parameters for elliptical vortex computations.

Parameter	Symbol	Gaussian, MMZ	POLY	Smooth Kirchhoff
Computational domain $[-L, L]^2$	L	3.2	6.4	12.8
Number of focusing levels	n_f	4	3	4
Focusing subdomains $[-r_i, r_i]^2$	r_i	3.2, 3, 2.6, 2.2	6.4, 5.2, 4	12.8, 10, 7.5, 5
Focusing mesh sizes	h_i	0.2, 0.1, 0.05, 0.025	0.2, 0.1, 0.05	0.8, 0.4, 0.2, 0.1
Number of AMR levels	n_{AMR}	2	2	2
AMR tolerances	ϵ_1, ϵ_2	(1, 0.70), (1, 0.75)	0.8, 0.45	0.8, 0.25
Time step	Δt	0.001	0.001	0.002
Kernel smoothing parameter	δ	0.1	0.1	0.1

regular mesh, the vorticity is interpolated from the old particles to the new particles, and the calculation proceeds.

In the present work the vorticity at the new particles is computed using bicubic polynomial interpolation in each panel,

$$p(x, y) = \sum_{i=0}^3 \sum_{j=0}^3 c_{ij} (x - x_c)^i (y - y_c)^j, \quad (10)$$

where (x_c, y_c) is the panel center defined by averaging the four panel vertices. The coefficients c_{ij} are determined by interpolating the vorticity at the 16 particles in the panel,

$$p(\mathbf{x}_\ell^{\text{old}}) = \omega_\ell^{\text{old}}, \quad \ell = 1:16, \quad (11)$$

where the superscript *old* denotes the particle location and vorticity before remeshing. Equation (11) yields a linear system which is solved for the coefficients c_{ij} , and the vorticity at the new particles is obtained by interpolation,

$$\omega(\mathbf{x}_\ell^{\text{new}}) = p(\mathbf{x}_\ell^{\text{new}}), \quad \ell = 1:16. \quad (12)$$

To carry out the last step, each new particle $\mathbf{x}_\ell^{\text{new}}$ is located in a unique panel associated with the old particles; this is done by searching the old panels for the one that minimizes the distance, $|\mathbf{x}_\ell^{\text{new}} - \mathbf{x}_c^{\text{old}}|$, between the new particle and the old panel centers. In the present calculations remeshing is done every time step.

C. Convergence study

Next we present a convergence study of the remeshed vortex method described above for circular Gaussian, MMZ, POLY, and smooth Kirchhoff vortices; this is the case $r^2 = x^2 + y^2$ in Eq. (7). In the exact solution the vorticity is radially symmetric and independent of time, and the particles rotate with angular velocity dependent on their radius.

The computational domain is $[-1.6, 1.6]^2$, which contains the compact MMZ and POLY vortices, and is large enough to ensure that truncating the noncompact Gaussian and SK vortices induces negligible error. Solutions were computed with panels of mesh size $h = 0.2, 0.1, 0.05, 0.025$. The smoothing parameter for the SK profile in Eq. (7d) is $\delta = 0.1$, and for particle time-stepping in Eq. (9) it is $\delta = 4h$. We record the max-norm vorticity error,

$$e_{\text{max}}^h = \frac{\max_i |\omega_i^h - \omega_0(\mathbf{x}_i)|}{\max_i |\omega_0(\mathbf{x}_i)|}, \quad (13)$$

where the maximum is taken over all panel vertex particles \mathbf{x}_i , $\omega_0(\mathbf{x}_i)$ is the exact particle vorticity, and ω_i^h is the particle vorticity computed with mesh size h . Remeshing is done every time step, and the time step is $\Delta t = 0.001$, which is small enough to ensure that the temporal discretization

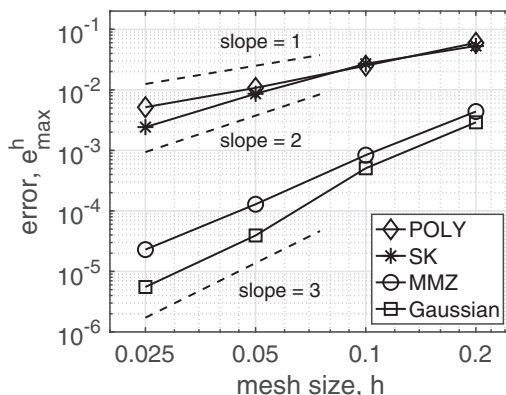


FIG. 5. Convergence of remeshed vortex method for circular vortices, error e_{\max}^h versus mesh size h at time $t = 1$, Gaussian, MMZ, POLY, smooth Kirchhoff vortices, smoothing parameter $\delta = 0.1$ in Eq. (7d), and particle time-stepping with $\delta = 4h$ in Eq. (9).

error is negligible. Hence e_{\max}^h measures the spatial discretization error which has two sources, the two-point Gaussian quadrature applied to the panel integrals and the bicubic interpolation used for remeshing.

Figure 5 shows the error e_{\max}^h versus mesh size h at time $t = 1$. For all four profiles, the error decreases as the mesh is refined. Dashed lines indicate convergence at the rate $O(h^p)$ for $p = 1, 2, 3$. Based on the two finest meshes, the observed convergence rates are $p = 1.06$ for the POLY vortex, $p = 1.83$ for the SK vortex, $p = 2.49$ for the MMZ vortex, and $p = 2.83$ for the Gaussian vortex.

Several factors affect the convergence rate. In principle, two-point Gaussian quadrature and bicubic interpolation are fourth-order accurate on square panels, but the panel shape distorts slightly in each time step and this reduces the convergence rate. Another factor is the regularity of the vorticity profile. The low convergence rate for the POLY profile is attributed to its discontinuous derivative [Fig. 2(g)]. The SK vortex has the next highest convergence rate; the profile is analytic but has a steep gradient and high curvature, and there is a transition from $p \approx 1$ for a coarse mesh to $p \approx 2$ for a fine mesh. The MMZ profile has the next highest convergence rate; the profile is infinitely differentiable but not analytic at the edge. Finally, the Gaussian profile is everywhere analytic with moderate steepness and curvature, and it has the highest convergence rate. Overall the results confirm the convergence of the remeshed vortex method with respect to spatial refinement.

D. Domain focusing and adaptive mesh refinement

The remeshed vortex method described above uses uniform panels, but this is inefficient for simulating elliptical vortices which require a large computational domain and develop small-scale features. To address this we employ domain focusing and adaptive mesh refinement.

Assume the vortex is centered at the origin. Domain focusing employs a sequence of uniform meshes with decreasing mesh size h_i on nested square subdomains $[-r_i, r_i]^2$ for $i = 1 : n_f$, where n_f is the number of focusing levels. Figure 6 shows an example with three focusing levels; level 1 panels have mesh size h_1 on the entire domain $[-r_1, r_1]^2$, level 2 panels have mesh size h_2 on subdomain $[-r_2, r_2]^2$, and level 3 panels have mesh size h_3 on subdomain $[-r_3, r_3]^2$. We employ dyadic subdivision with mesh spacing $h_{i+1} = h_i/2$, and hence the process yields a fine mesh near the origin and a progressively coarser mesh further away.

Adaptive mesh refinement (AMR) was developed to improve the efficiency of fluid dynamics simulations, originally for finite-difference schemes [55,56] and later also for particle methods

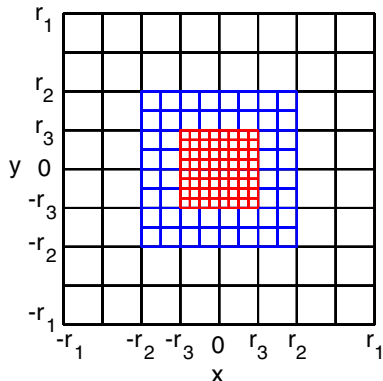


FIG. 6. Example of domain focusing with three levels, mesh size h_i on domain $[-r_i, r_i]^2$, $i = 1, 2, 3$, level 1 panels (black), level 2 panels (blue), and level 3 panels (red).

[57–59]. In the present work we employ two AMR criteria on each panel,

$$|\omega_{\max} - \omega_{\min}| \leq \epsilon_1, \quad \frac{|\omega_{\max} - \omega_{\min}|}{|\omega_{\max}|} \leq \epsilon_2, \quad (14)$$

where ω_{\max} , ω_{\min} are the maximum and minimum vorticity over the 16 particles in the panel, and $\epsilon_{1,2}$ are user-specified tolerances; these criteria control the absolute and relative vorticity variation in the panel. The AMR process is applied recursively to each panel in the focused mesh; if a panel violates either criterion, then it is refined, subject to a specified maximum number n_{AMR} of AMR levels. The refinement bisects the panel in the x and y directions, creating four child subpanels each with its own 4×4 particle grid whose vorticity is interpolated from the parent panel. A final check ensures that neighbor panels differ by at most one level. The resulting panels have an adaptive quadtree structure [36,60,61].

The particle and panel data are stored in arrays. The particle array contains the particle locations \mathbf{x}_i and vorticity ω_i . Each entry in the panel array contains the panel side length and refinement level, a flag indicating whether the panel has children, indices of the child panels, indices of the neighbor panels, and indices of the particles belonging to the panel. Note that some vertex and edge particles belong to more than one panel, but they are not duplicated in the particle array; when a panel is refined, the neighbor panels are checked to see whether the new vertex and edge particles already exist.

E. Treecode

The most time-consuming part of the calculation is computing the particle velocities in Eq. (9). With N particles the cost using direct summation scales like $O(N^2)$, and hence we employ a Cartesian Taylor treecode which reduces the cost to $O(N \log N)$. The treecode organizes the particles into a quadtree of clusters, and the well-separated particle-particle interactions are computed by a particle-cluster approximation, while the nearby particle-particle interactions are computed directly [62–64]. The computations were done on an iMac desktop computer with eight 2.3-GHz Intel Xeon cores and the treecode was parallelized using MPI.

VI. NUMERICAL RESULTS

Table I presents the numerical parameters used for the elliptical vortex computations. These values were obtained by trial and error to ensure that the numerical results are converged to within plotting accuracy. In these examples the vorticity either has compact support or vanishes rapidly at

infinity; the computational domain $[-L, L]^2$ encompasses the separatrix and a buffer region so that the vorticity at the boundary is less than $1e-10$ and this cut-off has negligible effect on the results. Hence the Gaussian and MMZ vortices have the smallest domain, while the POLY and SK vortices have larger domains. The computations extend over the time interval $0 \leq t \leq 10$ and the results are plotted using ParaView. In the following figures only a subdomain surrounding each vortex is shown. In addition to the figures, movies in the supplementary material show the evolution of the vortices and adaptively refined panels [65].

A. Gaussian vortex

Figure 7 shows the evolution of the Gaussian vortex, where column 1 shows the vorticity down to amplitude $\omega = 1e-3$, column 2 shows the logarithm of vorticity $\ln \omega$, and column 3 shows the adaptively refined panels. At time $t = 0$, the vorticity and its logarithm appear as diffuse elliptical patches. The AMR scheme produces two patches of refined panels on the slopes of the core where the vorticity profile is steepest. The center of the vortex was not refined because the vorticity variation there is small.

At time $t = 1$ the core has become more circular and two filaments with low-amplitude vorticity emerge from the tips of the rotating core. Recall that Fig. 3 showed the initial phase portraits of the elliptical vortices in a corotating frame, with two hyperbolic points h_1, h_2 and their stable and unstable manifolds, and we expect these features to persist in time. Hence the filamentation is attributed to vorticity advection along the outer branches of the unstable manifolds [25,28]; one filament moves from h_1 to h_2 along s_{12}^o and the other moves from h_2 to h_1 along s_{21}^o ; note however that this advection occurs in a corotating frame, so in the nonrotating physical frame the filaments amount to weak vorticity left behind by the rapidly rotating core.

At time $t = 3$ the core has become even more circular, while the filaments are longer and form spirals winding around inside and outside the core, as shown more clearly in Fig. 8. The inner portions of the filaments are attributed to vorticity advection along the inner branches of the unstable manifolds, s_{12}^i, s_{21}^i ; these portions of the filaments are harder to see because they have relatively small vorticity variation in comparison to the core vorticity, but the AMR scheme detected this variation and refined the panels accordingly. More precisely, the AMR scheme refines the sides the filaments, where the vorticity variation is relatively large, rather than the filament plateau where it is relatively small.

At time $t = 6$ the core remains nearly axisymmetric and the filaments have more turns separated by channels of weak vortical fluid. At time $t = 10$ the core is surrounded by a halo of nearly circular spiral filaments, but two small lobes with low-amplitude vorticity are present within the halo; these are shown more clearly in Fig. 9. The movie shows what happened; the vortex core starts to oscillate noticeably past time $t = 6$, and the lobes develop gradually by a local accumulation of weak vortical fluid in the channels between the filaments. The lobes seen here resemble features seen in simulations of vortex sheet roll-up (Fig. 4 in Ref. [66]), and as in that case we attribute them to a resonance stemming from the core oscillation.

B. MMZ vortex

Figure 10 shows the evolution of the MMZ vortex. As for the Gaussian vortex, the core becomes more circular in time and is surrounded by a halo of thin filaments with low-amplitude vorticity, but unlike the Gaussian vortex, the MMZ vortex core remains elliptical and the halo has a different structure.

At time $t = 0$, the vorticity and its logarithm appear as elliptical patches. A thin ring of refined panels is present around the edge of the vortex where the vorticity profile has high curvature, and two patches of refined panels appear on the slopes of the core where the profile is steepest.

At time $t = 1$ two filaments with low-amplitude vorticity emerge, but they are longer and thinner than for the Gaussian vortex. Recall from Fig. 3(b) that the hyperbolic points h_1, h_2 in the corotating

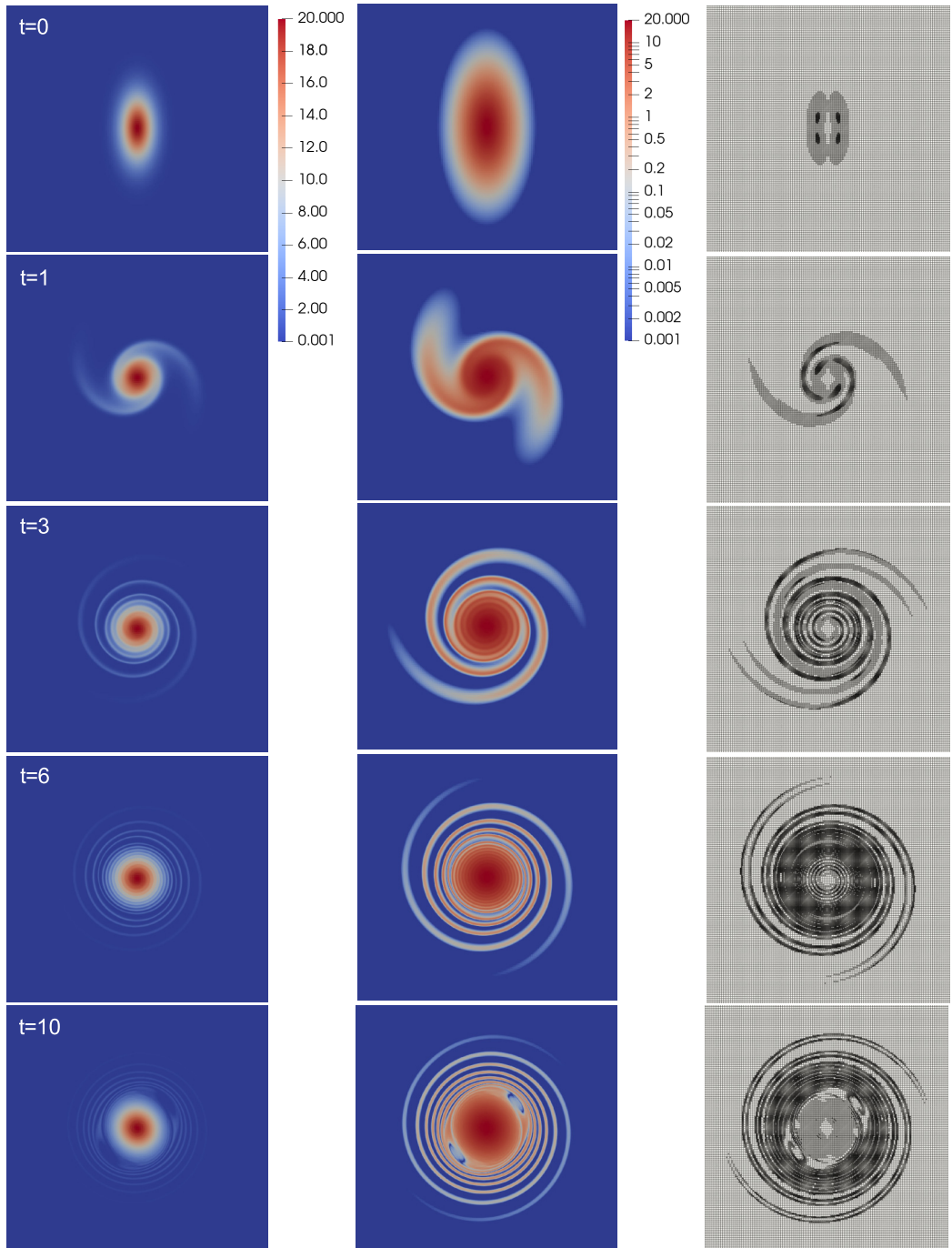


FIG. 7. Gaussian vortex, time $0 \leq t \leq 10$, column 1: vorticity ω , column 2: logarithm of vorticity $\ln \omega$, column 3: panels, subdomain shown is $[-1.725, 1.725]^2$, see the movie in the supplementary material [65].

frame lie inside the vortex [25,28], and hence the filaments are again attributed to vorticity advection along the outer branches of the unstable manifolds, s_{12}^o, s_{21}^o .

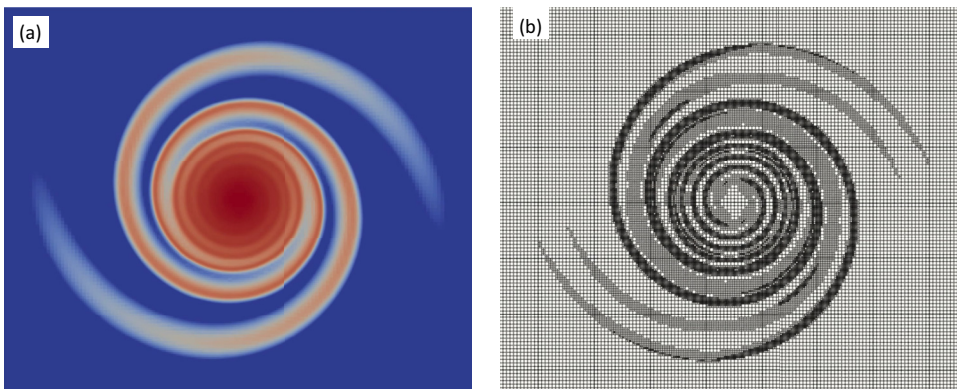


FIG. 8. Gaussian vortex, time $t = 3$; (a) logarithm of vorticity and (b) panels, subdomain shown is $[-1.65, 1.65]^2$.

At time $t = 3$ portions of the filament emerging from h_1 have reached the vicinity of h_2 , and similarly for the other filament, and in this way the filaments entrain irrotational fluid to form two crescent-shaped lobes next to the core, similarly to the phase portrait in Fig. 3(b). This is in contrast to the Gaussian vortex, but as in that case the filaments extend inside the core as shown more clearly in Fig. 11, and this is again attributed to vorticity advection along the inner branches of the unstable manifolds, s_{12}^i, s_{21}^i .

At time $t = 6$ the core and lobes form a rotating tripole surrounded by filaments, while at time $t = 10$ the lobes have become smaller and the filaments have more turns. The movie shows how the lobes become smaller; after the lobes form, they are stretched around the core, the rear of each lobe opens up, and some irrotational fluid is detrained from the lobe into the halo. We surmise that this detrainment process repeats in time, and as the lobes become depleted of fluid, the structure tends to axisymmetrize.

To understand this better recall the four invariant regions in the corotating phase portraits of the elliptical vortices in Fig. 1 and Fig. 3, comprising the center, two lobes, and exterior. In a steady flow like the Kirchhoff vortex, the stable manifold of one hyperbolic point coincides with the unstable manifold of the other point, and there is no exchange of fluid among the regions. However, in

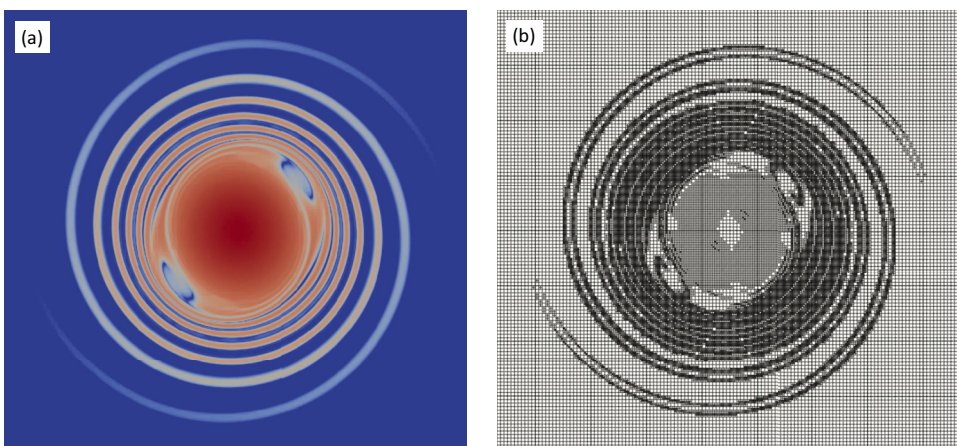


FIG. 9. Gaussian vortex, time $t = 10$; (a) logarithm of vorticity and (b) panels, subdomain shown is $[-1.5, 1.5]^2$.

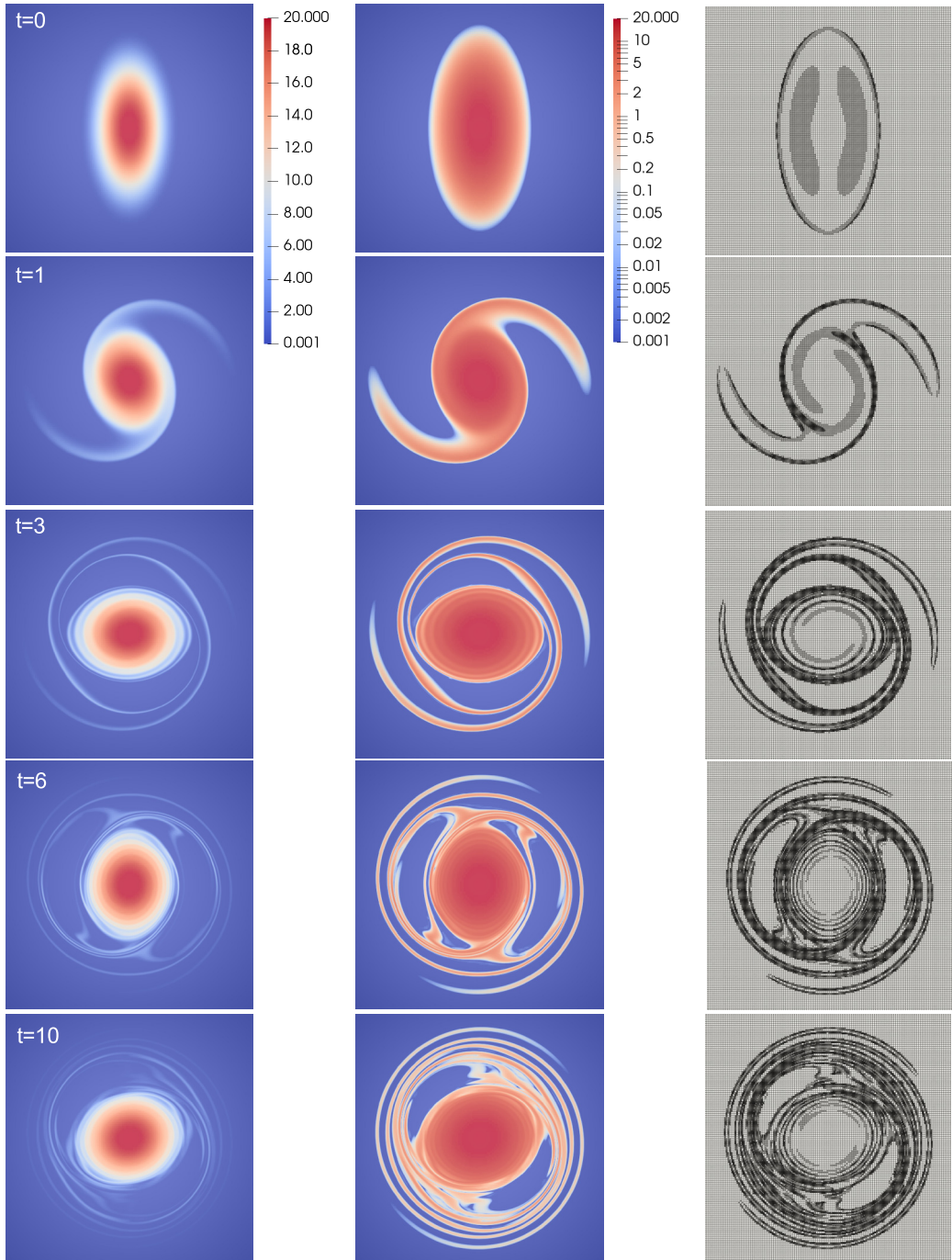


FIG. 10. MMZ vortex, time $0 \leq t \leq 10$. Column 1: vorticity ω ; column 2: logarithm of vorticity $\ln \omega$; column 3: panels; subdomain shown is $[-1.725, 1.725]^2$; see the movie in the supplementary material [65].

an unsteady flow like the MMZ vortex, the stable and unstable manifolds can intersect to form a heteroclinic tangle, and this permits vorticity to be advected from one region to another [47–50]; we

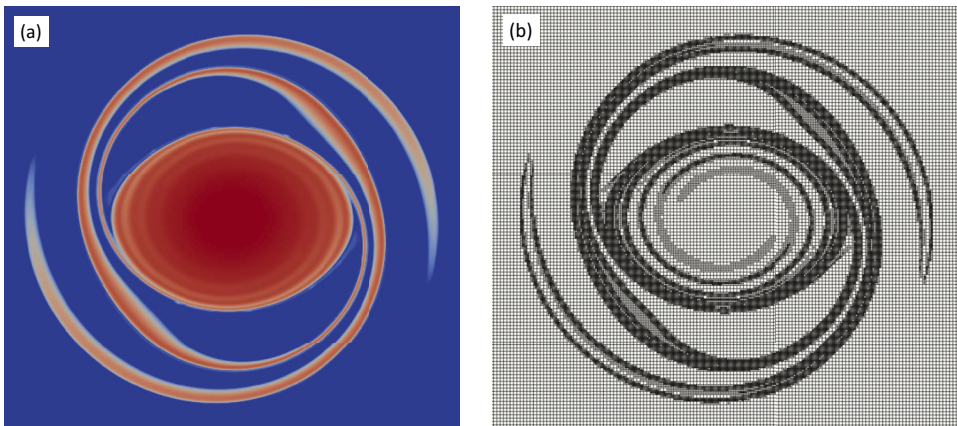


FIG. 11. MMZ vortex, time $t = 3$. (a) Logarithm of vorticity and (b) panels; subdomain shown is $[-1.75, 1.75]^2$.

surmise that this is the mechanism behind the repeated detrainment of fluid from the lobes into the halo.

C. POLY vortex

Figure 12 shows the evolution of the POLY vortex which is generally similar to that of the MMZ vortex, with filaments forming a halo outside the core and entrainment of irrotational fluid into crescent-shaped lobes. At time $t = 1$ the POLY vortex nearly retains its initial 2:1 aspect ratio, while the outer filaments are thinner than those of the MMZ vortex. At time $t = 3$ the POLY vortex lobes are similar in size and shape to the lobes in the initial phase portrait in Fig. 3(c). The panels show some trace of filaments winding around the slopes of the core, but they are clustered near the edge of the core because the inner branches of the unstable manifolds, s_{12}^i, s_{21}^i , lie close to the edge of the vortex in Fig. 3(c). At time $t = 6$ the rear of each lobe has opened up and some irrotational fluid is being detrained from the lobe into the halo. The movie shows that by time $t = 6.5$, the lobe closes and the detrainment stops, but another detrainment occurs around time $t = 9$. Although detrainment reduces the lobe area, at time $t = 10$ the POLY lobes remain larger than the MMZ lobes. Throughout the evolution, the POLY vortex core retains a nearly 2:1 aspect ratio, while the halo oscillates between nearly circular and oval shapes; this is in contrast to the Gaussian and MMZ vortices whose core and halo evolve to be closer to circular.

D. Smooth Kirchhoff vortex

Figure 13 shows the evolution of the smooth Kirchhoff vortex. The vorticity in column 1 shows that the core rotates without much change in shape, similarly to the exact Kirchhoff vortex, but the logarithm of vorticity in column 2 shows significant structure outside the core. At time $t = 0$ the relatively slow decay of vorticity away from the core causes the logarithm of vorticity to appear diffuse. At time $t = 1$ two filaments emerge and wrap around the core as before, although here they have a long tail of smoothly varying weak vorticity. By time $t = 3$ a tripole structure has formed, although in this case the lobes enclose weak vortical fluid. At time $t = 6$ the filaments form nearly circular spiral turns outside the core and lobes. The movie shows that the lobes open up and detrainment occurs around time $t = 5$ and $t = 8$. At time $t = 10$ the core has changed only slightly from its initial size and aspect ratio. A thin band of low-amplitude vorticity $\omega \approx 0.5$ surrounds the separatrix, and the outer filaments have nearly circular spiral turns with lower amplitude vorticity. In previous cases we saw that the filaments extend inside the core; we surmise that this happens here,

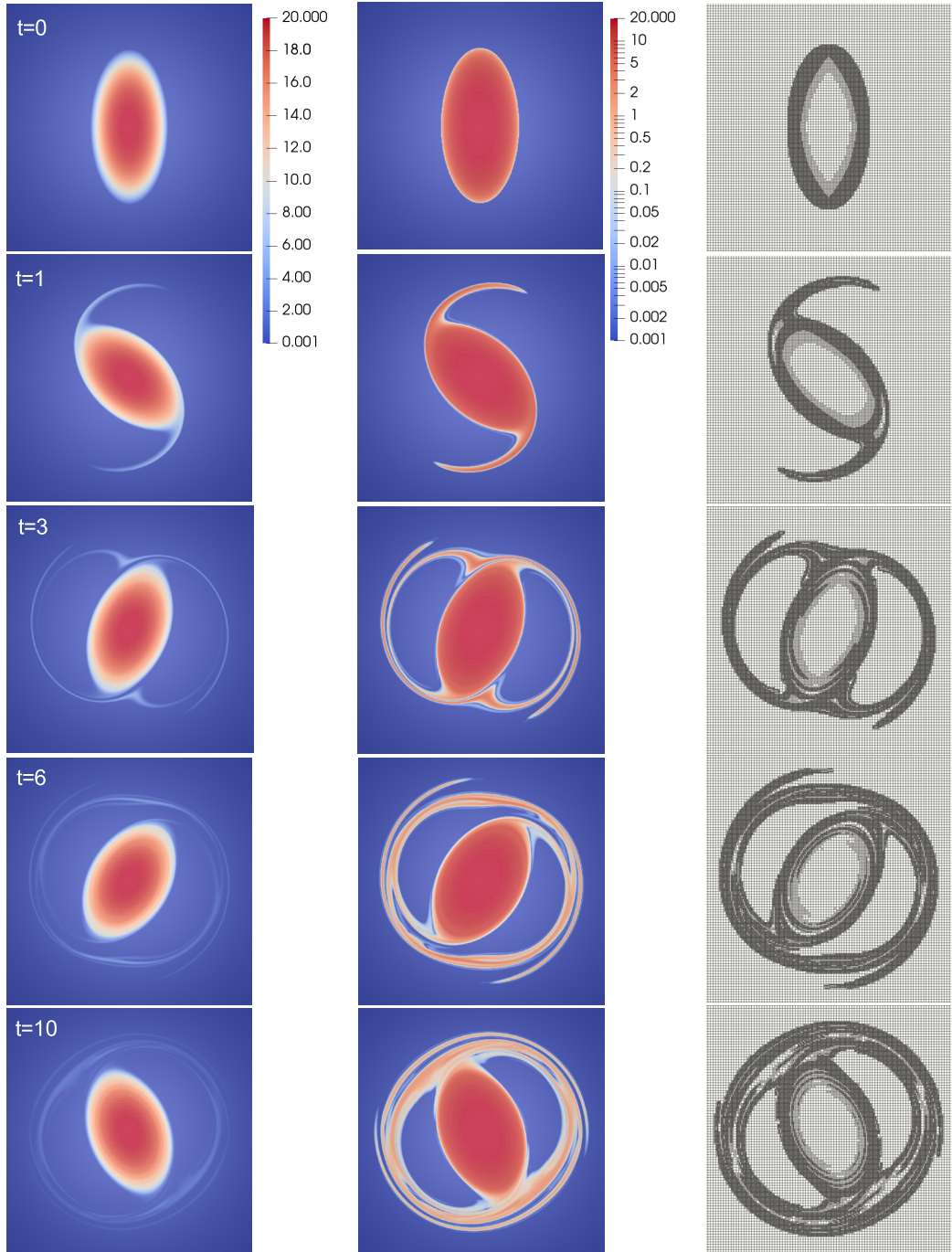


FIG. 12. POLY vortex, time $0 \leq t \leq 10$. Column 1: vorticity, ω ; column 2: logarithm of vorticity, $\ln \omega$; column 3: panels. Subdomain shown is $[-2.4, 2.4]^2$; see the movie in the supplementary material [65].

too, but these vorticity variations are barely visible, although their presence is indirectly indicated by the dense panel refinement near the edge of the core.

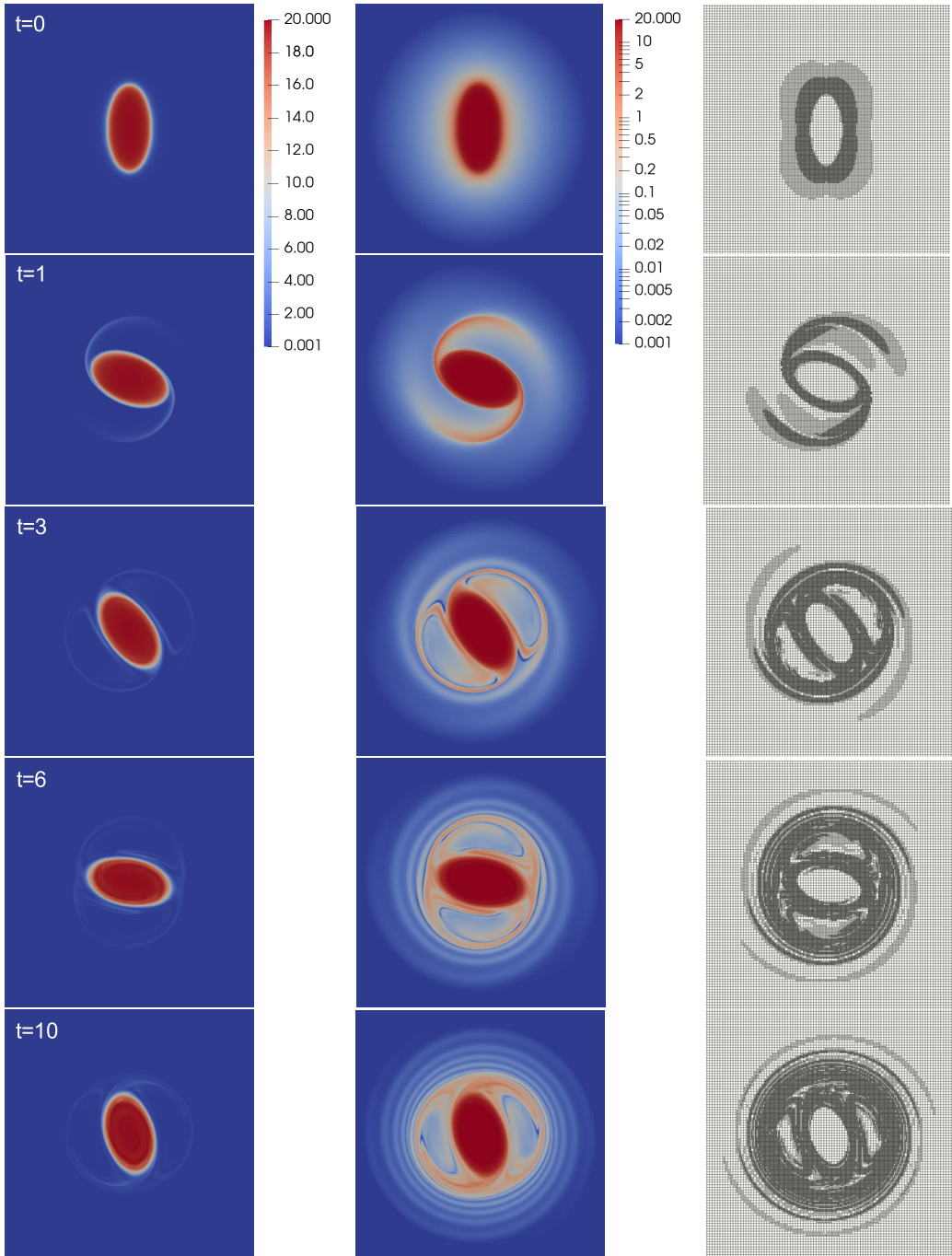


FIG. 13. Smooth Kirchhoff vortex, time $0 \leq t \leq 10$. Column 1: vorticity, ω ; column 2: logarithm of vorticity, $\ln \omega$; column 3: panels. Subdomain shown is $[-4.8, 4.8]^2$; see the movie in the supplementary material [65].

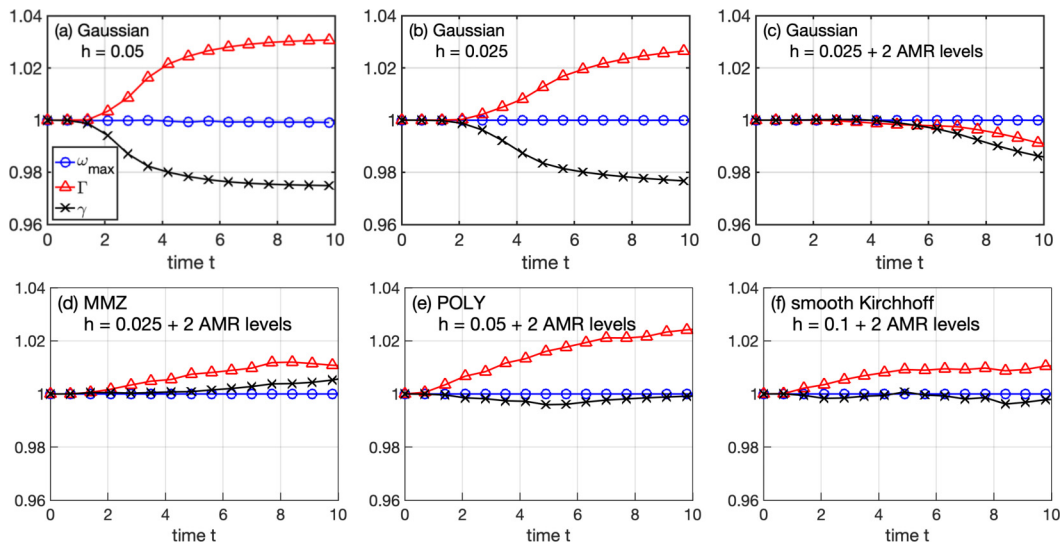


FIG. 14. Conserved quantities relative to their initial value, vorticity maximum ω_{\max} (\circ , blue), circulation Γ (Δ , red), enstrophy γ (\times , black), time $0 \leq t \leq 10$, [(a)–(c)] Gaussian vortex, frames (a) and (b) use uniform mesh size h as indicated, (d) MMZ vortex, (e) POLY vortex, (f) smooth Kirchhoff vortex, and [(c)–(f)] with mesh size h and AMR levels as in Table I.

VII. CONSERVED QUANTITIES

Here we consider several invariant conserved quantities for the Euler equations comprising the maximum vorticity ω_{\max} , total circulation Γ , and total enstrophy γ ,

$$\omega_{\max}(t) = \max_{\mathbf{x} \in \mathbb{R}^2} \omega(\mathbf{x}, t), \quad \Gamma(t) = \int_{\mathbb{R}^2} \omega(\mathbf{x}, t) d\mathbf{x}, \quad \gamma(t) = \int_{\mathbb{R}^2} \omega^2(\mathbf{x}, t) d\mathbf{x}. \quad (15)$$

Figure 14 shows the computed values relative to the initial values for time $0 \leq t \leq 10$. The top three frames [Figs. 14(a)–14(c)] concern the Gaussian vortex, and they show the effect of the grid spacing h and AMR. The maximum vorticity ω_{\max} is well conserved in all cases, and while the circulation and enstrophy drift slightly in time, the deviation from exact conservation is less than 4% in all cases. The calculation becomes more accurate as the spatial discretization is refined from Figs. 14(a) to Fig. 14(b) to Fig. 14(c); while reducing the grid spacing h improves the accuracy, AMR is even more effective in enforcing conservation. Similar trends were observed for the MMZ, POLY, and smooth Kirchhoff vortices as seen in the bottom three frames. Using two levels of AMR, the deviation from exact conservation is less than 2.5% for all four vortices at the final time $t = 10$. These relatively small deviations may be taken to indicate the accuracy of the calculations.

VIII. EFFECT OF SMOOTHING PARAMETER

The vortex method implemented here uses a regularized Biot-Savart kernel with smoothing parameter δ as indicated in Eq. (9); this yields a regularized version of the Euler equations and the exact Euler solution is recovered in the limit $\delta \rightarrow 0$. However, in practice it is difficult to accurately resolve the solution for small δ and hence the elliptical vortex calculations in Sec. VI used the value $\delta = 0.1$, but this naturally raises a question about the effect this has on the results.

Figure 15 addresses this question by comparing results with three smoothing parameter values, $\delta = 0.2$ (column 1), $\delta = 0.1$ (column 2), and $\delta = 0.05$ (column 3), where the MMZ vortex is used as a representative example and the logarithm of vorticity is plotted for time $t = 0, 1, 2, 3, 4$. It is clear that the large scales are not strongly affected by the value of δ , the main effect being that

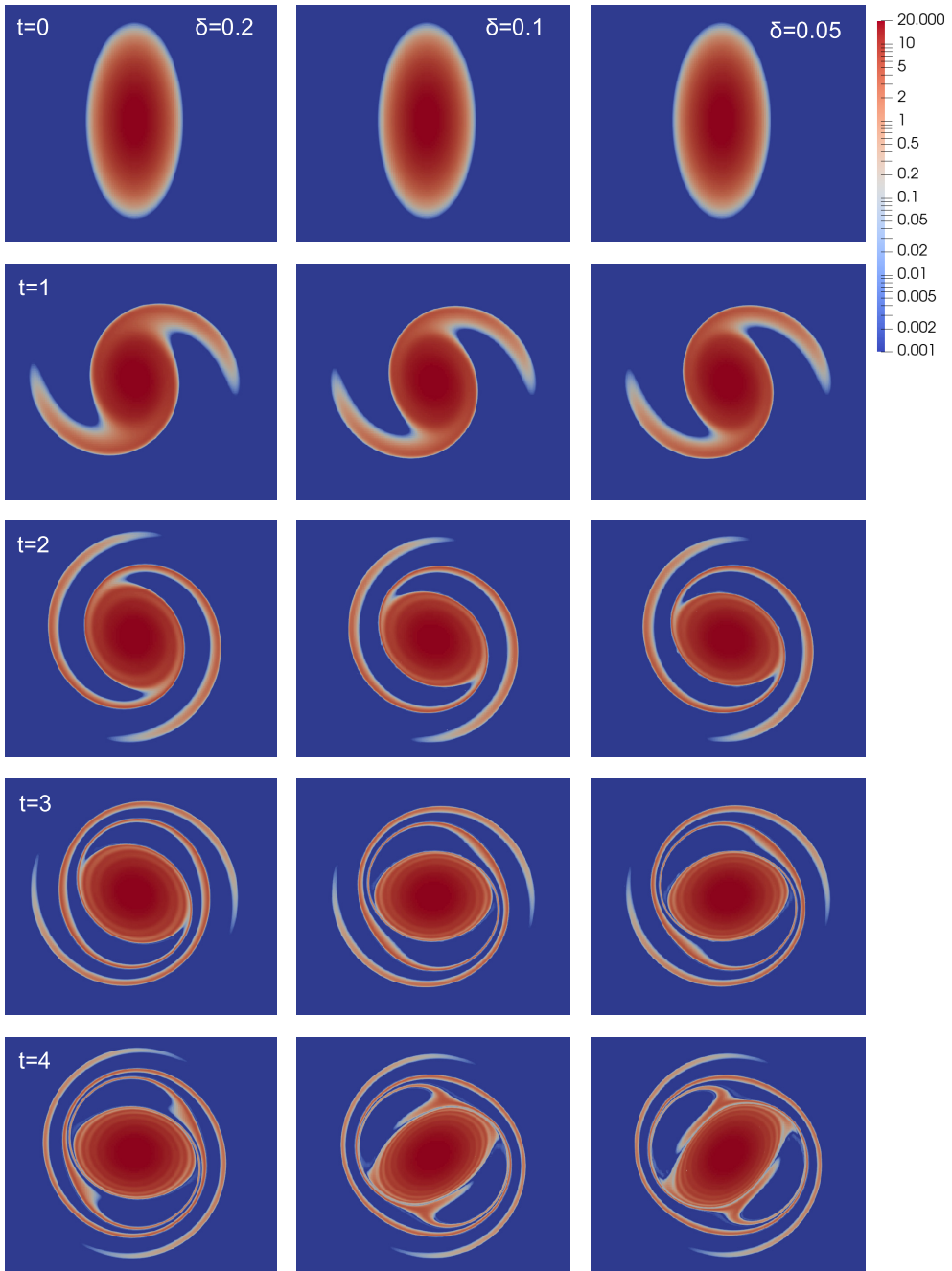


FIG. 15. Effect of smoothing parameter, MMZ vortex, logarithm of vorticity, time $t = 0, 1, 2, 3, 4$, subdomain shown is $[-2.2, 2.2]^2$, column 1: $\delta = 0.2$, column 2: $\delta = 0.1$, and column 3: $\delta = 0.05$.

the evolution is somewhat slower for larger δ , but the sequence of events (filamentation, lobe, and halo formation) is similar for the different values of δ . Concerning the small scales, for example the width of the filaments, here too, the value of δ does not have a strong effect. The results in Fig. 15 are all well resolved, but extending the $\delta = 0.05$ calculation to time $t = 10$ would require higher

resolution and be substantially more expensive. Nonetheless the evidence suggests that the $\delta = 0.1$ calculation gives an accurate approximate picture of the true Euler dynamics in the limit $\delta \rightarrow 0$.

IX. SUMMARY

This work examined the dynamics of elliptical vortices in 2D ideal fluid using an adaptively refined and remeshed vortex method. Four examples were considered comprising the compact MMZ [25] and POLY vortices [29], and noncompact Gaussian and SK vortices. The vortices have the same maximum vorticity and 2:1 initial aspect ratio, but unlike the top-hat Kirchhoff vortex, they have continuous profiles although with different regularity.

In each case the phase portrait of the vortex in a corotating frame has two hyperbolic points, and the separatrix divides space into four regions, a center containing the vortex core, two crescent-shaped lobes next to the core, and the exterior. As the vortices start to rotate, two spiral filaments emerge and form a halo of low-amplitude vorticity around the core; this filamentation is attributed to vorticity advection along the unstable manifolds of the hyperbolic points [25,28,32]. Afterwards there are two scenarios.

In the case of the Gaussian vortex, the core rapidly axisymmetrizes and the filaments form nearly circular spirals, but a steady state is not reached; instead, the core starts to oscillate, fluid accumulates locally in the channels between the filaments, and two small lobes enclosing weak vortical fluid form within the halo; this is attributed to a resonance stemming from the core oscillation. In this way the emergence of lobes from a nearly axisymmetric state opposes axisymmetrization.

In the case of the MMZ, POLY, and SK vortices, something different happens; the core remains elliptical for longer time, and the filaments entrain fluid into two large lobes next to the core. The resulting nonaxisymmetric tripole has an elliptical core, two crescent-shaped lobes enclosing irrotational (MMZ, POLY) or weakly vortical fluid (SK), and a halo of nearly circular spiral filaments around the core and lobes. The structure resembles the separatrix in the corotating frame, but it is unsteady; the lobes repeatedly open up at the rear, detrain some of their fluid into the halo and then close up again; this is attributed to a heteroclinic tangle near the hyperbolic points [47–50]. In this way the lobes are gradually depleted of fluid thereby promoting axisymmetrization, although this happens faster for the MMZ vortex than for the POLY and SK vortices.

There is a striking contrast between the rapid axisymmetrization of the Gaussian vortex and the persistent core ellipticity in the MMZ, POLY, and SK vortices. It is notable that the Gaussian profile has high curvature at the center and essentially no plateau, while the other three profiles are almost flat near the center with progressively wider plateaus. The idea that profile curvature at the vortex center plays a critical role in determining the rate of inviscid axisymmetrization was already seen in the asymptotic analysis of Bassom and Gilbert [18].

In summary we found several competing tendencies, some that promote axisymmetrization (filamentation, depletion of lobes), and others that oppose it (flatness of core plateau, emergence of lobes). While it has been suggested that elliptical vortices could evolve to either an axisymmetric monopole state or a nonaxisymmetric tripole state, it may be that a steady state is not reached as the core oscillates in time, and lobes repeatedly form, are depleted, and re-form. The dynamics may resemble to some extent the top-hat Kirchhoff vortex in a strain field [67], where, however, in the present case the strain is self-induced rather than externally imposed. Future longer time calculations may clarify these issues using more powerful algorithms and computing hardware [68]. Another potential application for the vortex method described here is to the control of externally driven vortices [10,11,69].

ACKNOWLEDGMENTS

This work was supported by the MCubed program and the Michigan Institute for Computational Discovery and Engineering (MICDE) at the University of Michigan. The authors thank Peter Bosler for helpful discussions.

-
- [1] H. Lamb, *Hydrodynamics* (Cambridge University Press, Cambridge, UK, 1924).
- [2] P. G. Saffman, *Vortex Dynamics* (Cambridge University Press, Cambridge, UK, 1995).
- [3] A. E. H. Love, On the stability of certain vortex motions, *Proc. Lond. Math. Soc.* **s1-25**, 18 (1893).
- [4] N. J. Zabusky, M. Hughes, and K. Roberts, Contour dynamics for the Euler equations in two dimensions, *J. Comput. Phys.* **30**, 96 (1979).
- [5] D. I. Pullin, Contour dynamics methods, *Annu. Rev. Fluid Mech.* **24**, 89 (1992).
- [6] T. Mitchell and L. Rossi, The evolution of Kirchhoff elliptic vortices, *Phys. Fluids* **20**, 054103 (2008).
- [7] J. F. Lingeitch and A. J. Bernoff, Distortion and evolution of a localized vortex in an irrotational flow, *Phys. Fluids* **7**, 1015 (1995).
- [8] B. Legras, D. G. Dritschel, and P. Caillol, The erosion of a distributed two-dimensional vortex in a background straining flow, *J. Fluid Mech.* **441**, 369 (2001).
- [9] M. R. Turner and A. D. Gilbert, Linear and nonlinear decay of cat's eyes in two-dimensional vortices, and the link to Landau poles, *J. Fluid Mech.* **593**, 255 (2007).
- [10] N. C. Hurst, J. R. Danielson, D. H. E. Dubin, and C. M. Surko, Adiabatic behavior of an elliptical vortex in a time-dependent external strain flow, *Phys. Rev. Fluids* **6**, 054703 (2021).
- [11] P. Wongwaitayakornkul, J. Danielson, N. Hurst, D. Dubin, and C. Surko, Inviscid damping of an elliptical vortex subject to an external strain flow, *Phys. Plasmas* **29**, 052107 (2022).
- [12] P. Orlandi and G. F. van Heijst, Numerical simulation of tripolar vortices in 2D flow, *Fluid Dyn. Res.* **9**, 179 (1992).
- [13] G. J. F. van Heijst, R. C. Kloosterziel, and C. W. M. Williams, Laboratory experiments on the tripolar vortex in a rotating fluid, *J. Fluid Mech.* **225**, 301 (1991).
- [14] R. J. Briggs, J. D. Daugherty, and R. H. Levy, Role of Landau damping in crossed-field electron beams and inviscid shear flow, *Phys. Fluids* **13**, 421 (1970).
- [15] C. F. Driscoll and K. S. Fine, Experiments on vortex dynamics in pure electron plasmas, *Phys. Fluids B: Plasma Physics* **2**, 1359 (1990).
- [16] D. A. Schecter, D. H. E. Dubin, A. C. Cass, C. F. Driscoll, I. M. Lansky, and T. M. O'Neil, Inviscid damping of asymmetries on a two-dimensional vortex, *Phys. Fluids* **12**, 2397 (2000).
- [17] A. J. Bernoff and J. F. Lingeitch, Rapid relaxation of an axisymmetric vortex, *Phys. Fluids* **6**, 3717 (1994).
- [18] A. P. Bassom and A. D. Gilbert, The spiral wind-up of vorticity in an inviscid planar vortex, *J. Fluid Mech.* **371**, 109 (1998).
- [19] S. Le Dizès, Non-axisymmetric vortices in two-dimensional flows, *J. Fluid Mech.* **406**, 175 (2000).
- [20] N. J. Balmforth, S. G. Llewellyn Smith, and W. R. Young, Disturbing vortices, *J. Fluid Mech.* **426**, 95 (2001).
- [21] I. M. Hall, A. P. Bassom, and A. D. Gilbert, The effect of fine structure on the stability of planar vortices, *Eur. J. Mech. B Fluid* **22**, 179 (2003).
- [22] M. R. Turner and A. D. Gilbert, Thresholds for the formation of satellites in two-dimensional vortices, *J. Fluid Mech.* **614**, 381 (2008).
- [23] N. Whitaker and B. Turkington, Maximum entropy states for rotating vortex patches, *Phys. Fluids* **6**, 3963 (1994).
- [24] J. Bedrossian, M. Coti Zelati, and V. Vicol, Vortex axisymmetrization, inviscid damping, and vorticity depletion in the linearized 2D Euler equations, *Ann. PDE* **5**, 4 (2019).
- [25] M. V. Melander, J. C. McWilliams, and N. J. Zabusky, Axisymmetrization and vorticity-gradient intensification of an isolated two-dimensional vortex through filamentation, *J. Fluid Mech.* **178**, 137 (1987).
- [26] D. G. Dritschel, Contour surgery: A topological reconnection scheme for extended integrations using contour dynamics, *J. Comput. Phys.* **77**, 240 (1988).
- [27] D. G. Dritschel, Contour dynamics and contour surgery: Numerical algorithms for extended, high-resolution modelling of vortex dynamics in two-dimensional, inviscid, incompressible flows, *Comput. Phys. Rep.* **10**, 77 (1989).
- [28] L. M. Polvani, G. R. Flierl, and N. J. Zabusky, Filamentation of unstable vortex structures via separatrix crossing: A quantitative estimate of onset time, *Phys. Fluids A: Fluid Dynamics* **1**, 181 (1989).
- [29] P. Koumoutsakos, Inviscid axisymmetrization of an elliptical vortex, *J. Comput. Phys.* **138**, 821 (1997).

- [30] L. F. Rossi, J. F. Lingeitch, and A. J. Bernoff, Quasi-steady monopole and tripole attractors for relaxing vortices, *Phys. Fluids* **9**, 2329 (1997).
- [31] D. G. Dritschel, On the persistence of non-axisymmetric vortices in inviscid two-dimensional flows, *J. Fluid Mech.* **371**, 141 (1998).
- [32] O. V. Fuentes, Vortex filamentation: Its onset and its role on axisymmetrization and merger, *Dynam. Atmos. Oceans* **40**, 23 (2005).
- [33] L. A. Barba and A. Leonard, Emergence and evolution of tripole vortices from net-circulation initial conditions, *Phys. Fluids* **19**, 017101 (2007).
- [34] R. Pakter and Y. Levin, Nonequilibrium statistical mechanics of two-dimensional vortices, *Phys. Rev. Lett.* **121**, 020602 (2018).
- [35] C. A. F. Farias, R. Pakter, and Y. Levin, Linear and non-linear instabilities of Kirchhoff's elliptical vortices, *J. Stat. Mech. Theory Exp.* (2020) 083205.
- [36] P. Bosler, L. Wang, C. Jablonowski, and R. Krasny, A Lagrangian particle/panel method for the barotropic vorticity equations on a rotating sphere, *Fluid Dyn. Res.* **46**, 031406 (2014).
- [37] P. A. Bosler, J. Kent, R. Krasny, and C. Jablonowski, A Lagrangian particle method with remeshing for tracer transport on the sphere, *J. Comput. Phys.* **340**, 639 (2017).
- [38] A. J. Chorin, Numerical study of slightly viscous flow, *J. Fluid Mech.* **57**, 785 (1973).
- [39] A. Leonard, Vortex methods for flow simulation, *J. Comput. Phys.* **37**, 289 (1980).
- [40] G.-H. Cottet and P. D. Koumoutsakos, *Vortex Methods: Theory and Practice*, Vol. 8 (Cambridge University Press, Cambridge, UK, 2000).
- [41] C. Mimeau and I. Mortazavi, A review of vortex methods and their applications: From creation to recent advances, *Fluids* **6**, 68 (2021).
- [42] O. H. Hald, Convergence of vortex methods for Euler's equations. II, *SIAM J. Numer. Anal.* **16**, 726 (1979).
- [43] J. T. Beale and A. Majda, Vortex methods. II. Higher order accuracy in two and three dimensions, *Math. Comp.* **39**, 29 (1982).
- [44] M. Perlman, On the accuracy of vortex methods, *J. Comput. Phys.* **59**, 200 (1985).
- [45] D. Wee and A. F. Ghoniem, Modified interpolation kernels for treating diffusion and remeshing in vortex methods, *J. Comput. Phys.* **213**, 239 (2006).
- [46] A. J. Chorin and J. E. Marsden, *A Mathematical Introduction to Fluid Mechanics*, Texts in Applied Mathematics, Vol. 4 (Springer-Verlag, Berlin, 1993).
- [47] A. L. Bertozzi, Heteroclinic orbits and chaotic dynamics in planar fluid flows, *SIAM J. Math. Anal.* **19**, 1271 (1988).
- [48] V. Rom-Kedar, A. Leonard, and S. Wiggins, An analytical study of transport, mixing and chaos in an unsteady vortical flow, *J. Fluid Mech.* **214**, 347 (1990).
- [49] L. M. Polvani and J. Wisdom, Chaotic Lagrangian trajectories around an elliptical vortex patch embedded in a constant and uniform background shear flow, *Phys. Fluids A: Fluid Dynamics* **2**, 123 (1990).
- [50] K. Ide and S. Wiggins, The dynamics of elliptically shaped regions of uniform vorticity in time-periodic, linear external velocity fields, *Fluid Dyn. Res.* **15**, 205 (1995).
- [51] C. K. Birdsall and A. B. Langdon, *Plasma Physics via Computer Simulation* (CRC Press, Boca Raon, FL, 2018).
- [52] J.-L. Vay, P. Colella, P. McCorquodale, B. Van Straalen, A. Friedman, and D. Grote, Mesh refinement for particle-in-cell plasma simulations: Applications to and benefits for heavy ion fusion, *Laser Part. Beams* **20**, 569 (2002).
- [53] B. Wang, G. H. Miller, and P. Colella, A particle-in-cell method with adaptive phase-space remapping for kinetic plasmas, *SIAM J. Sci. Comput.* **33**, 3509 (2011).
- [54] A. Magni and G.-H. Cottet, Accurate, non-oscillatory, remeshing schemes for particle methods, *J. Comput. Phys.* **231**, 152 (2012).
- [55] M. J. Berger and J. Olinger, Adaptive mesh refinement for hyperbolic partial differential equations, *J. Comput. Phys.* **53**, 484 (1984).
- [56] M. J. Berger and P. Colella, Local adaptive mesh refinement for shock hydrodynamics, *J. Comput. Phys.* **82**, 64 (1989).

- [57] M. Bergdorf, G.-H. Cottet, and P. Koumoutsakos, Multilevel adaptive particle methods for convection-diffusion equations, *Multiscale Model. Sim.* **4**, 328 (2005).
- [58] P. Koumoutsakos, Multiscale flow simulations using particles, *Annu. Rev. Fluid Mech.* **37**, 457 (2005).
- [59] D. Rossinelli, B. Hejazialhosseini, W. van Rees, M. Gazzola, M. Bergdorf, and P. Koumoutsakos, MRAG-I2D: Multi-resolution adapted grids for remeshed vortex methods on multicore architectures, *J. Comput. Phys.* **288**, 1 (2015).
- [60] H. Feng, L. Kaganovskiy, and R. Krasny, Azimuthal instability of a vortex ring computed by a vortex sheet panel method, *Fluid Dyn. Res.* **41**, 051405 (2009).
- [61] D. Kolomenskiy, J.-C. Nave, and K. Schneider, Adaptive gradient-augmented level set method with multiresolution error estimation, *J. Sci. Comput.* **66**, 116 (2016).
- [62] J. Barnes and P. Hut, A hierarchical $O(N \log N)$ force-calculation algorithm, *Nature (Lond.)* **324**, 446 (1986).
- [63] K. Lindsay and R. Krasny, A particle method and adaptive treecode for vortex sheet motion in three-dimensional flow, *J. Comput. Phys.* **172**, 879 (2001).
- [64] P. Li, H. Johnston, and R. Krasny, A Cartesian treecode for screened Coulomb interactions, *J. Comput. Phys.* **228**, 3858 (2009).
- [65] See supplemental material at <http://link.aps.org/supplemental/10.1103/PhysRevFluids.8.024702> for multimediafiles.
- [66] R. Krasny and M. Nitsche, The onset of chaos in vortex sheet flow, *J. Fluid Mech.* **454**, 47 (2002).
- [67] S. Kida, Motion of an elliptic vortex in a uniform shear flow, *J. Phys. Soc. Jpn.* **50**, 3517 (1981).
- [68] L. Wilson, N. Vaughn, and R. Krasny, A GPU-accelerated fast multipole method based on barycentric Lagrange interpolation and dual tree traversal, *Comput. Phys. Commun.* **265**, 108017 (2021).
- [69] M. A. Borich and L. Friedland, Driven chirped vorticity holes, *Phys. Fluids* **20**, 086602 (2008).